

Flower-like Hierarchical $\text{Ti}_3\text{C}_2\text{T}_x@\text{MoS}_2/\text{Nitrogen-doped Carbon Composite}$ as High-performance Anodes for Sodium-ion Batteries

Guangsheng Dong,^[a] Lixin Li,^[a] Penghui Cui,^[a] A. M. A. Mohamed,^[a] Kai Zhu,^{*[a, b]} and Dianxue Cao^{*[a]}

The lack of high-performance electrodes is a key factor restricting the development of sodium-ion batteries (SIBs), and usually a certain type of electrode material alone often fails to combine the merits of high capacity and good conductivity. Herein, nitrogen-doped carbon (NC) was used as a multifunctional bridge to uniformly compound high-capacity MoS_2 nanoparticles with highly conductive $\text{Ti}_3\text{C}_2\text{T}_x$ nanosheets to form $\text{Ti}_3\text{C}_2\text{T}_x@\text{MoS}_2/\text{NC}$ composite with flower-like architecture. Ultrafine MoS_2 nanoparticles were uniformly anchored on $\text{Ti}_3\text{C}_2\text{T}_x$ nanosheets to form nanosheets primary building blocks with a sandwich-like architecture, which not only shortens the ion transfer distance but also enlarges the layer spacing of $\text{Ti}_3\text{C}_2\text{T}_x$

favoring the storage of more sodium ions as well as their transport capacity. Moreover, the flower-like structures with abundant edges can provide an ample active sites and high pseudocapacitance behavior. As a result, flower-like $\text{Ti}_3\text{C}_2\text{T}_x@\text{MoS}_2/\text{NC}$ displays a high electrochemical properties with an excellent cycling stability over 2000 cycles (81.4% capacity retention) and preeminent rate capacity of 383 mAh g^{-1} at 30 A g^{-1} . Furthermore, $\text{Ti}_3\text{C}_2\text{T}_x@\text{MoS}_2/\text{NC}||\text{Na}_3\text{V}_2(\text{PO}_4)_3$ full cell displays a capacity of 59 mAh g^{-1} at 0.4 A g^{-1} after 180 cycles. This work displays a high-performance anode composite for SIBs and provides insight into the preparation of other composites.

Introduction

In the face of growing energy demand and serious environmental pollution problems, the use of green renewable energy is imperative, and electrochemical energy storage technology is one of the critical technologies to address the intermittency and volatility of renewable energy.^[1–3] Lithium-ion batteries (LIBs) are commonly used because of their satisfactory performance, which has led to the depletion of limited lithium mining resources, and therefore the cost of LIBs has been rising.^[4,5] As a result, sodium-ion batteries (SIBs) have received particular attention in recent years because sodium has similar properties to lithium but is more abundant and cheaper.^[6–8] Since the weight and radius of Na^+ is larger than that of Li^+ , graphite, a commercial LIB anode material with a small layer spacing, is not

suitable for sodium storage.^[9,10] In addition, the large size of the Na^+ inevitably leads to hysteresis reaction kinetics and a tremendous volume expansion of the electrode materials during Na^+ insertion.^[11–13] Therefore, it becomes critical to explore novel high-performance anode materials to facilitate the early commercial production application of SIBs.

To improve the performance of SIBs, various alloying-type materials,^[14–17] transition metal oxides,^[18–20] transition metal sulfides,^[21–24] and other anode materials have been investigated. Among them, MXenes have attracted tremendous interest due to their ultra-high conductivity, unique layer structure, wide layer spacing and abundant tunable termination.^[25–28] However, since MXene is a insertion-type material, it can provide a lower specific capacity compared to alloying-type and conversion-type materials, and the susceptibility to re-stacking between neighboring nanosheets leads to a further reduction in its surface utilization, which seriously hampers its practical application.^[29,30] The compounding of MXenes with high-capacity materials not only increases the specific capacity of whole composites but also improves the stacking resistance of MXenes. Various MXene based composites have been successfully prepared and exhibit improved electrochemical performances.^[31–35] Yuan et al.^[31] obtained 3D cross-linked $\text{Nb}_2\text{CT}_x@\text{MoS}_2@\text{C}$ hybrid by hydrothermal anchoring of MoS_2 nanosheets on the Nb_2CT_x framework combined with PDA-derived carbon coating strategies. It displayed a high stability and capacity of 530 mAh g^{-1} at 0.1 A g^{-1} after 200 cycles with an ultra-low degradation of 0.01% per cycle. Yuan et al.^[32] wrapped $\text{Ti}_3\text{C}_2\text{T}_x$ on the surface of $\text{NiSe}_2@\text{C}$ spheres by an electrostatic assembly strategy, which effectively prevented the stacking of $\text{Ti}_3\text{C}_2\text{T}_x$ and thus improved its electrochemical

[a] G. Dong, L. Li, P. Cui, A. M. A. Mohamed, Dr. K. Zhu, Prof. D. Cao
Key Laboratory of Superlight Materials and Surface Technology (Ministry of Education)
College Material Science and Chemical Engineering Harbin Engineering University
Harbin 150001 (P. R. China)
E-mail: kzhu@hrbeu.edu.cn
caodianxue@hrbeu.edu.cn

[b] Dr. K. Zhu
Key Laboratory of Advanced Energy Materials Chemistry (Ministry of Education)
Nankai University
Tianjin 300071 (China)

 Supporting information for this article is available on the WWW under
<https://doi.org/10.1002/batt.202300391>

 An invited contribution to a Special Collection on Young Scientists in Battery Research.

properties. Han et al.^[33] prepared few-layered $\text{Ti}_3\text{C}_2/\text{CoS}_2@\text{NPC}$ with superior rate capability and long-term stability by carbonization and sulfurization treatment of f- $\text{Ti}_3\text{C}_2/\text{ZIF}-67$ composites. Yuan et al.^[34] synthesized $\text{Nb}_2\text{CT}_x/\text{MoS}_2@\text{CS}$ architectures with high capacity and rate performance by hydrothermal and electrostatic self-assembly approaches. Liu et al.^[35] successfully prepared the hierarchical 1T- $\text{MoS}_2/\text{MXene}$ heterostructure with large interlayer spacing and highly conductive by solvothermal method. The above results indicate that compositing MXene with high specific capacity materials to form composites can effectively improve the sodium storage performance of MXene.

Herein, we successfully anchored ultrafine MoS_2 with high theoretical specific capacity of 670 mAh g^{-1} on the surface of MXene nanosheet material with high electrical conductivity and cyclic stability to form a flower-like $\text{Ti}_3\text{C}_2\text{T}_x@\text{MoS}_2/\text{NC}$ composite by a combination of complexation, polymerization and sulfidation reactions. The complexation of molybdate with DA ensures a homogeneous compounding of the molybdenum source with DA and the nanosizing of the molybdenum source, which not only increases in material utilization but also effectively mitigates the volume variation during sodiation/desodiation progress. The polymerization reaction of DA in a weak alkaline environment firmly anchors the Mo source on the surface of $\text{Ti}_3\text{C}_2\text{T}_x$ nanosheets forming a sandwich-like architecture, which not only expands the layer spacing of $\text{Ti}_3\text{C}_2\text{T}_x$ for rapid ion transport but also effectively prevents its stacking. After the specific sulfidation reaction, the molybdenum source was successfully converted into MoS_2 nanoparticles and PDA into nitrogen-doped carbon (NC) as a linker to ensure good contact between MoS_2 nanoparticles and $\text{Ti}_3\text{C}_2\text{T}_x$ nanosheets to obtain high electrical conductivity. $\text{Ti}_3\text{C}_2\text{T}_x$ acts as the active material in the $\text{Ti}_3\text{C}_2\text{T}_x@\text{MoS}_2/\text{NC}$ complex while also acting as a skeleton support as well as providing a large active surface and high pseudocapacitive behavior. The as-prepared $\text{Ti}_3\text{C}_2\text{T}_x@\text{MoS}_2/\text{NC}$ composite combine the advantages of MoS_2 and $\text{Ti}_3\text{C}_2\text{T}_x$, combining high electrical conductivity and specific capacity with excellent cycling stability. Thus, it shows excellent rate property for sodium storage with a capacity of 383 mAh g^{-1} at 30 A g^{-1} . Meanwhile, it also exhibits stable cycling performance with a capacity of 351 mAh g^{-1} after 2000 cycles at 2 A g^{-1} . The corresponding capacity retention rate from the 20th cycle to the 2000th cycle is 81.4% with an extremely low capacity fade of 0.0103% per cycle.

Results and Discussion

Figure 1 proposes the synthesis process of the $\text{Ti}_3\text{C}_2\text{T}_x@\text{MoS}_2/\text{NC}$ composite. Firstly, $\text{Ti}_3\text{C}_2\text{T}_x$ nanosheets with larger size and fewer layers were successfully prepared by etching the Al atomic layers from Ti_3AlC_2 . Then, the nano-sized Mo source was anchored on the surface of $\text{Ti}_3\text{C}_2\text{T}_x$ nanosheets to form $\text{Ti}_3\text{C}_2\text{T}_x@\text{Mo/PDA}$ nanosheets with sandwich-like structure by complexation of molybdate with DA and polymerization of DA. Finally, the $\text{Ti}_3\text{C}_2\text{T}_x@\text{Mo/PDA}$ precursors were vulcanized to form $\text{Ti}_3\text{C}_2\text{T}_x@\text{MoS}_2/\text{NC}$ at high temperature in N_2 atmosphere.

Figure S1 shows that the sizes of the prepared few-layer $\text{Ti}_3\text{C}_2\text{T}_x$ nanosheets are concentrated in the range of tens to hundreds of microns. 2D $\text{Ti}_3\text{C}_2\text{T}_x$ nanosheets provide a large surface area which facilitates their surface utilization and the loading of other materials with high capacity on their surface. The $\text{Ti}_3\text{C}_2\text{T}_x@\text{Mo/PDA}$ primary building blocks with sandwich-like structure were formed by successfully anchoring the ultrafine Mo source on the surface of $\text{Ti}_3\text{C}_2\text{T}_x$ nanosheets using the polymerization and coating effect of DA. The formation of a sandwich-like structure not only expands the layer spacing of $\text{Ti}_3\text{C}_2\text{T}_x$ to improve ion transport channels but also prevents $\text{Ti}_3\text{C}_2\text{T}_x$ stacking. The addition of $\text{Ti}_3\text{C}_2\text{T}_x$ has an essential effect on the morphology of the precursor, as presented in Figure S2. When the addition amount of $\text{Ti}_3\text{C}_2\text{T}_x$ was 10 mg, the obtained precursors exhibit flower-like structures with sizes concentrated in 1–3 μm , and the thickness of their primary nanosheet assembly units was significantly thicker than pure $\text{Ti}_3\text{C}_2\text{T}_x$ (Figure S2a, b) this is due to the loading of a layer of MoS_2 nanoparticles on the surface of $\text{Ti}_3\text{C}_2\text{T}_x$. Increasing the addition of $\text{Ti}_3\text{C}_2\text{T}_x$ to 20 mg, the flower-like structure of the resulting $\text{Ti}_3\text{C}_2\text{T}_x@\text{Mo/PDA}$ precursor became less obvious (Figure S2c, d). When the introduction of $\text{Ti}_3\text{C}_2\text{T}_x$ was increased to 40 mg, the resulting product was in the form of tightly packed nanosheets rather than flower-like structure (Figure S2e, f). More importantly, the $\text{Ti}_3\text{C}_2\text{T}_x@\text{Mo/PDA}$ precursor has good structural thermal stability and maintains its original morphology and structure after high temperature vulcanization to $\text{Ti}_3\text{C}_2\text{T}_x@\text{MoS}_2/\text{NC}$ (Figure 2a, b and Figure S3). In view of the low theoretical specific capacity of $\text{Ti}_3\text{C}_2\text{T}_x$ and the best flower-like morphological structure of the product obtained when 10 mg of $\text{Ti}_3\text{C}_2\text{T}_x$ was introduced, the flower-like $\text{Ti}_3\text{C}_2\text{T}_x@\text{MoS}_2/\text{NC}$ was investigated in detail later.

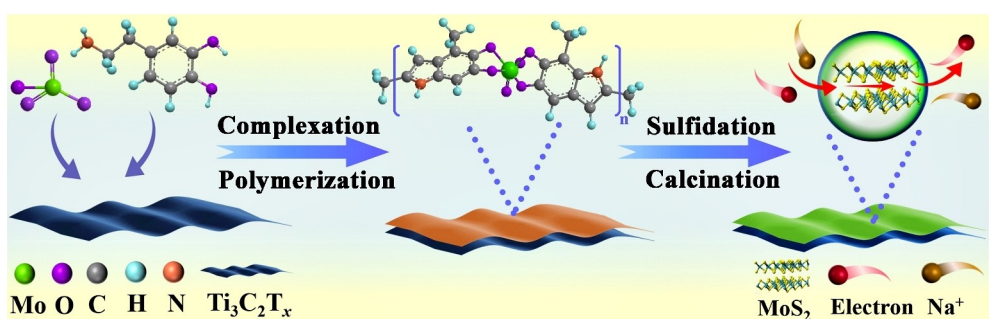


Figure 1. Schematic illustration of the preparation of the $\text{Ti}_3\text{C}_2\text{T}_x@\text{MoS}_2/\text{NC}$ composite.

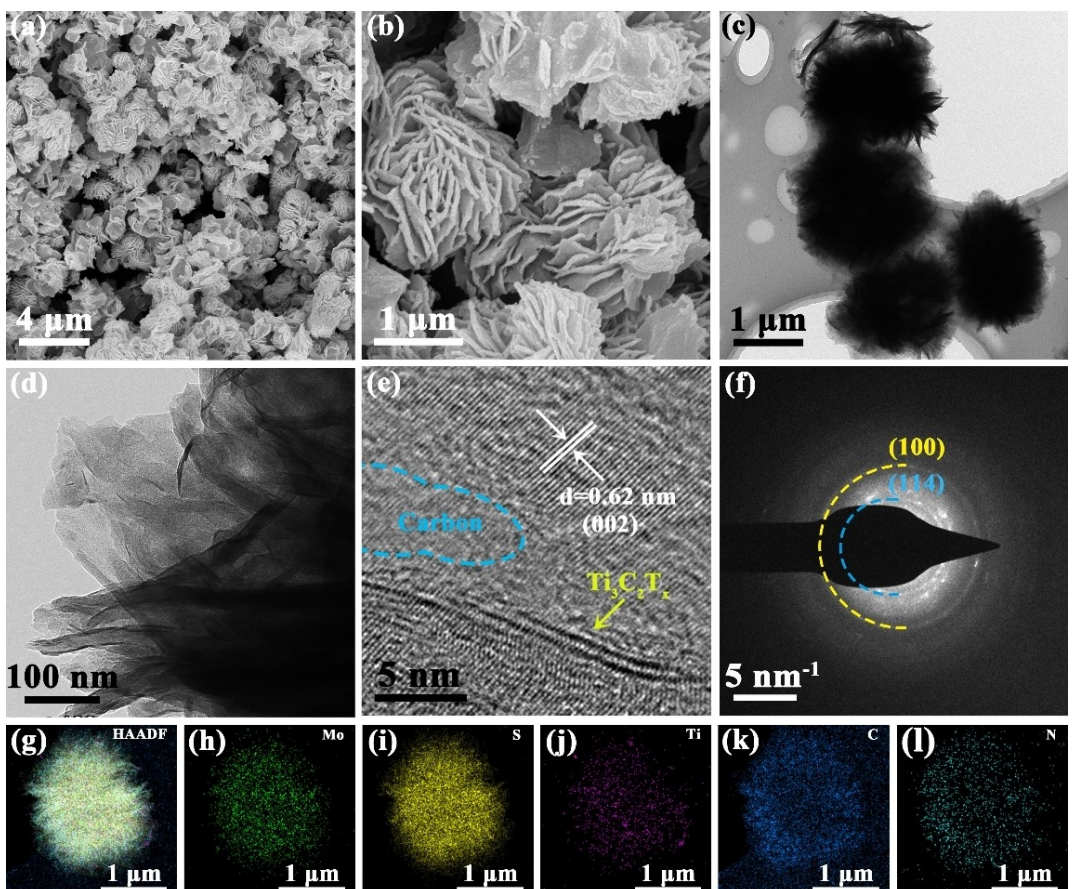


Figure 2. a, b) SEM images, c, d) TEM images, e) HRTEM image, f) SAED pattern, g–l) TEM element mapping of the flower-like $\text{Ti}_3\text{C}_2\text{T}_x@\text{MoS}_2/\text{NC}$.

The SEM images of the flower-like $\text{Ti}_3\text{C}_2\text{T}_x@\text{MoS}_2/\text{NC}$ show that the assembled units are nanosheets and their thickness is significantly larger than that of $\text{Ti}_3\text{C}_2\text{T}_x$ (Figure 2a, b). The increase of the nanosheet thickness indicates the successful cladding of MoS_2/NC layers on the surface of $\text{Ti}_3\text{C}_2\text{T}_x$ nanoflakes. The flower-like structure formed by interweaving nanosheets can expose more active surfaces and offer substantial sodium storage sites, while providing a smooth transport channel for Na^+ transport.^[37] The TEM results at low magnification are consistent with the SEM results, from which flower-like structures with rich margins can also be observed (Figure 2c, d). The clear lattice stripes with a spacing of 0.62 nm can be viewed from the high-resolution TEM image of $\text{Ti}_3\text{C}_2\text{T}_x@\text{MoS}_2/\text{NC}$ indicating the good crystallinity of the complex (Figure 2e). This distance is consistent with the (002) lattice spacing of MoS_2 ,^[38] indicating that the MoS_2 nanoparticles are successfully anchored to the $\text{Ti}_3\text{C}_2\text{T}_x$ nanosheets, which is consistent with the increased thickness of the $\text{Ti}_3\text{C}_2\text{T}_x$ nanosheets shown by the SEM results (Figure 2b). In addition, it can be observed in Figure 2(e) that the amorphous NC and superfine MoS_2 are uniform compounded on the surface of the few-layer $\text{Ti}_3\text{C}_2\text{T}_x$ nanoflakes, which not only enhances the utilisation of MoS_2 and $\text{Ti}_3\text{C}_2\text{T}_x$ but also effectively increases the conductivity of the overall electrode material. The characteristic diffraction rings of MoS_2 can be observed in the corresponding selected area

electron diffraction (SAED), indicating that the prepared MoS_2 has polycrystalline structural characteristics (Figure 2f). The EDS elemental distribution images of the flower-like $\text{Ti}_3\text{C}_2\text{T}_x@\text{MoS}_2/\text{NC}$ display an even distribution of five elements Mo, S, Ti, C and N, indicating that the MoS_2/NC layers are uniformly compounded with the $\text{Ti}_3\text{C}_2\text{T}_x$ nanosheets (Figure 2g–l). The close contact between MoS_2 nanoparticles and $\text{Ti}_3\text{C}_2\text{T}_x$ nanosheets and the homogeneous composite contribute to the enhancement of the specific capacity and electrical conductivity of the electrode materials. In addition, the $\text{Ti}_3\text{C}_2\text{T}_x@\text{MoS}_2/\text{NC}$ hierarchical structure is assembled from nanosheets with sandwich-like structure formed by porous NC anchoring ultrasmall MoS_2 nanoparticles on the surface of $\text{Ti}_3\text{C}_2\text{T}_x$ nanosheets, and thus it has a large specific surface area of $118 \text{ m}^2 \text{ g}^{-1}$ as well as abundant mesoporous structure, which is conducive for it to provide a high surface pseudocapacitance behavior as well as a fast ion transport (Figure S4).

Figure 3(a) illustrates the XRD spectrum of the flower-like $\text{Ti}_3\text{C}_2\text{T}_x@\text{MoS}_2/\text{NC}$, from which the characteristic diffraction peaks of MoS_2 can be identified indicating the successful loading of MoS_2 . Furthermore, compared with the pure $\text{Ti}_3\text{C}_2\text{T}_x$, the (002) peak position of $\text{Ti}_3\text{C}_2\text{T}_x@\text{MoS}_2/\text{NC}$ shifts down from $2\theta = 7.2^\circ$ to 5.6° (Figure 3a), demonstrating that the disorder and interlayer spacing of $\text{Ti}_3\text{C}_2\text{T}_x$ significantly increased after anchoring with MoS_2/NC , which is consistent with the SEM

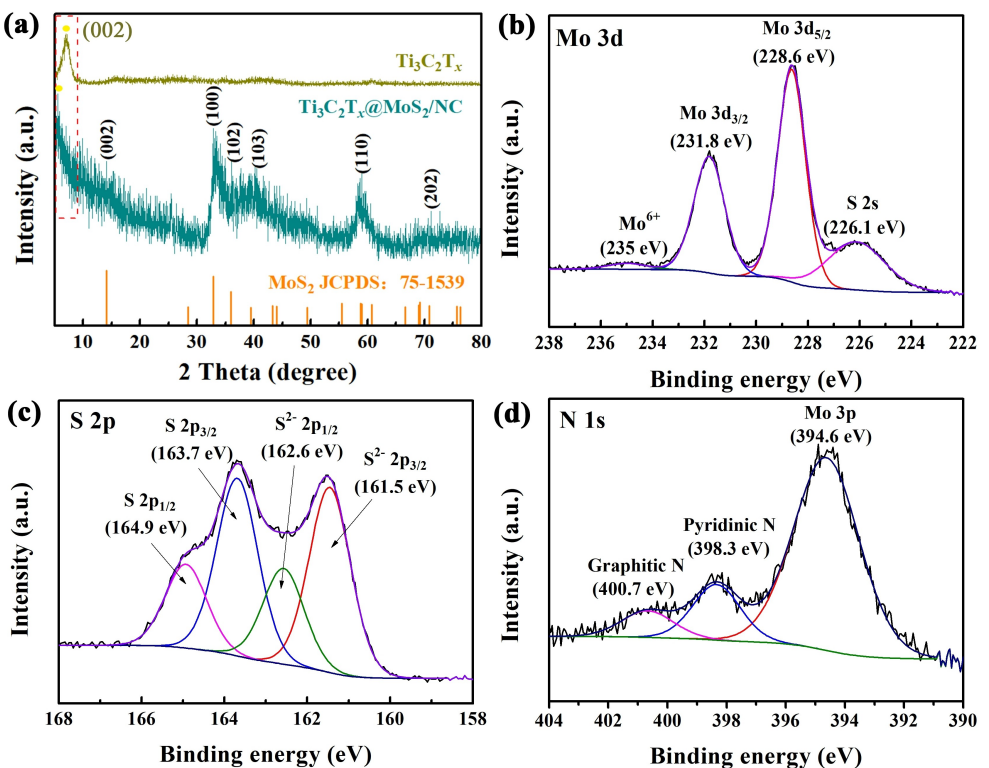


Figure 3. a) XRD patterns of the flower-like $\text{Ti}_3\text{C}_2\text{T}_x@\text{MoS}_2/\text{NC}$ and $\text{Ti}_3\text{C}_2\text{T}_x$, XPS spectra of $\text{Ti}_3\text{C}_2\text{T}_x@\text{MoS}_2/\text{NC}$ for b) Mo 3d, c) S 2p, d) N 1s.

results.^[39] $\text{Ti}_3\text{C}_2\text{T}_x$ with larger layer spacing can offer more sodium storage sites and more fluent ion transport channels. Figure 3(b) demonstrates the high-resolution XPS spectrum of Mo 3d, where the peaks at wt 228.6 and 231.8 eV can be attributed to $\text{Mo } 3\text{d}_{5/2}$ and $\text{Mo } 3\text{d}_{3/2}$ of Mo^{4+} , respectively.^[40,41] The remaining diffraction peaks located at 226.1 and 235 eV positions are attributed to S 2 s and Mo^{6+} , respectively [40, 41]. There are two pairs of diffraction peaks in the S 2p spectrum, one pair at 161.5 and 162.6 eV are attributed to $2\text{p}_{3/2}$ and $2\text{p}_{1/2}$ of S^{2-} ^[42] and the other pair at 163.7 and 164.9 eV are assigned to $2\text{p}_{3/2}$ and $2\text{p}_{1/2}$ of S (Figure 3c),^[43] respectively. The presence of S is caused by a small amount of S remaining on the sample surface during the high temperature vulcanization process. The N 1s spectrum displays the peaks of graphitic N (400.7) and pyridine N (398.3 eV),^[44,45] which can further increase the electrical conductivity of the composites due to the large number of off-domain electrons available from the lone pairs of electrons they possess (Figure 3d). In addition, the remaining derivative peak at 394.6 eV in the N 1s spectrum is a Mo 3p diffraction peak.

Figure 4(a) shows the CV curve of the flower-like $\text{Ti}_3\text{C}_2\text{T}_x@\text{MoS}_2/\text{NC}$ at 0.5 mVs⁻¹ and a voltage range of 0.01–3 V for the original three cycles. There is a large irreversible reduction peak at 0.2 V in the first lap, which can be attributed to electrolyte decomposition forming solid electrolyte interface (SEI) film. The CV curves of the two subsequent turns almost overlap, indicating that the flower-like $\text{Ti}_3\text{C}_2\text{T}_x@\text{MoS}_2/\text{NC}$ electrode can be stabilized quickly. The reduction peak near 0.01 V can be ascribed to the generation of metallic Mo and Na_2S and

the insertion of Na^+ between the carbon and/or $\text{Ti}_3\text{C}_2\text{T}_x$ layers. The oxidation peak at 0.075 V is assigned to the detachment of Na^+ from the carbon and/or $\text{Ti}_3\text{C}_2\text{T}_x$ layer, while the oxidation peak at 1.8 V is indexed to the oxidation of Mo and Na_2S to form MoS_2 . Figure 4(b) demonstrates the initial three GCD curves of the flower-like $\text{Ti}_3\text{C}_2\text{T}_x@\text{MoS}_2/\text{NC}$ composite at 0.2 A g⁻¹ with initial charging and discharging reversible capacities of 734 and 926 mAh g⁻¹, respectively, accompanied by an initial Coulombic efficiency of 79.3%. Figure 4(c) shows the cycle capability comparison of the flower-like $\text{Ti}_3\text{C}_2\text{T}_x@\text{MoS}_2/\text{NC}$, $\text{Ti}_3\text{C}_2\text{T}_x$ and MoS_2 at 0.5 A g⁻¹. The $\text{Ti}_3\text{C}_2\text{T}_x@\text{MoS}_2/\text{NC}$ exhibited high specific capacity and cycling stability with a remaining specific capacity of 650 mAh g⁻¹ after 700 cycles. During the first few cycles, the capacity decreases rapidly due to the large amount of electrolyte consumed to form the SEI film and the fact that the active substances are not fully utilized. With the continuous charging and discharging, the active substance is fully utilized, and the specific capacity rises slowly until the capacity reaches the maximum value after 350 cycles, and then the capacity shows a regular slow decay trend. In comparison, the $\text{Ti}_3\text{C}_2\text{T}_x$ displays an excellent cycling stability but low specific capacity (~100 mAh g⁻¹). The MoS_2 exhibits a high specific capacity but a fast capacity decay. The $\text{Ti}_3\text{C}_2\text{T}_x@\text{MoS}_2/\text{NC}$ demonstrates high specific capacity and cycling stability can be attributed to its excellent composition and flower-like hierarchical structure. Moreover, the flower-like $\text{Ti}_3\text{C}_2\text{T}_x@\text{MoS}_2/\text{NC}$ exhibits a favorable rate performance obtaining average reversible specific capacities of 627, 621, 613, 601, 576, 534, 484, 434 and 383 mAh g⁻¹ at 0.2, 0.4, 0.8, 1.5, 3, 6, 12,

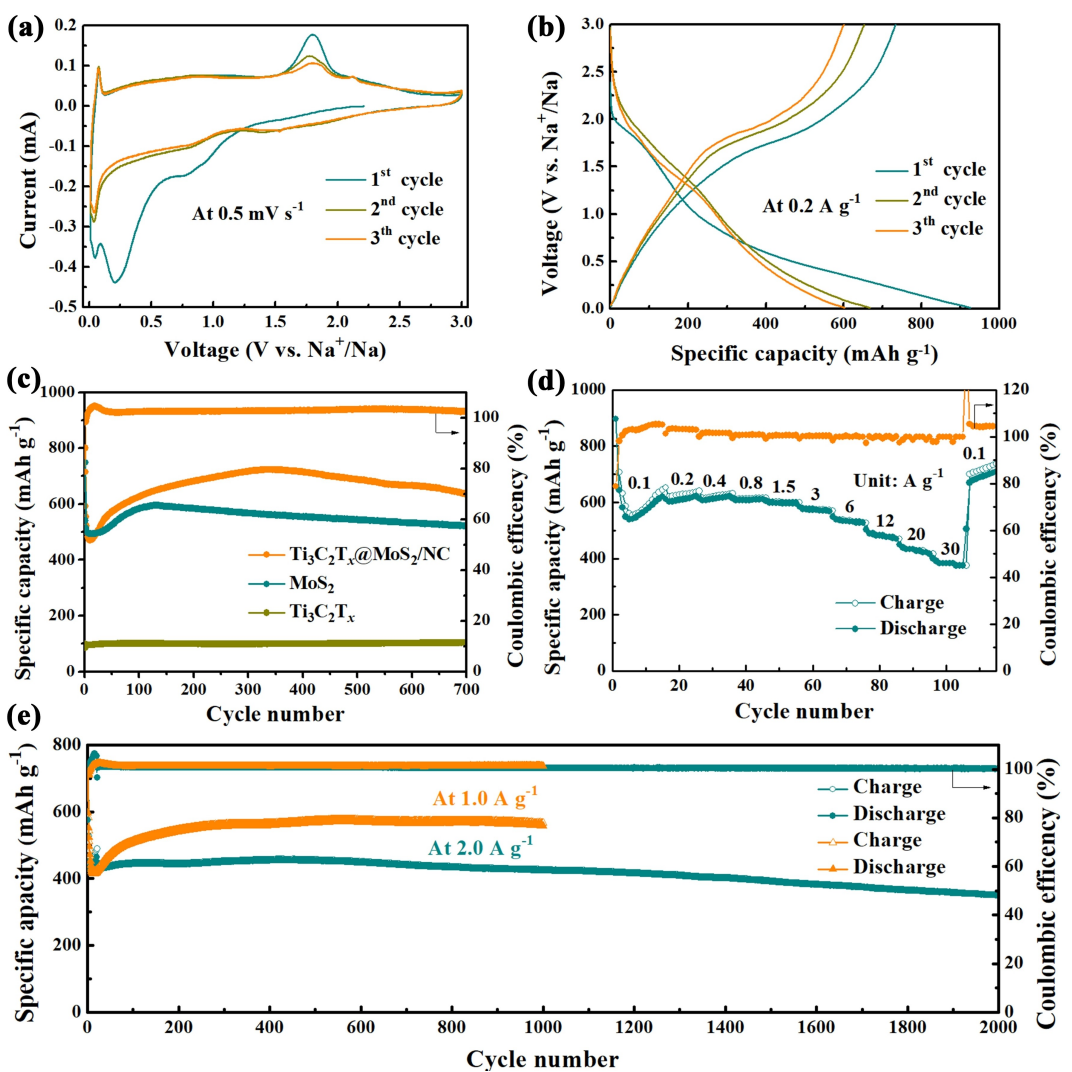


Figure 4. a) CV curves, b) GCD profiles, c) cycling performance comparison at 0.5 A g⁻¹, d) rate capability, e) long-term cycling stability at 1 and 2 A g⁻¹ of the flower-like Ti₃C₂T_x@MoS₂/NC.

20 and 30 A g⁻¹, respectively (Figure 4d). This can be ascribed to the multistage structure of the Ti₃C₂T_x@MoS₂/NC that provides smooth ion transport channels and the Ti₃C₂T_x that provides high electron transport rates. Furthermore, the flower-like Ti₃C₂T_x@MoS₂/NC also displays an acceptable cycling stability with a capacity of 558 mAh g⁻¹ was attained after 1000 cycles at 1 A g⁻¹. The capacity maintained at 351 mAh g⁻¹ after 2000 stabilization cycles at 2 A g⁻¹. The corresponding capacity retention during the 20th to 2000th cycles was 81.4% accompanied by an average capacity decay of 0.03% per cycle. As-prepared Ti₃C₂T_x@MoS₂/NC composite exhibits good sodium storage properties compared to similar materials reported in the literature (Table S1). The superior electrochemical properties of flower-like Ti₃C₂T_x@MoS₂/NC compared to pure Ti₃C₂T_x (Figure S5) are due to its better component composition and morphological structure.

To further investigate the reason for the excellent electrochemical properties of the flower-like Ti₃C₂T_x@MoS₂/NC, the pseudocapacitive behavior was analyzed after 10 cycles of

activation at 0.2 A g⁻¹ as indicated in Figure 5. Figure 5(a) shows the CV curve of Ti₃C₂T_x@MoS₂/NC at different sweep speeds from 0.2 to 1.0 mV s⁻¹. The position of the redox peaks shifted very little as the scan rate increased, which demonstrates that the polarization of the electrode materials is very small and it has the ability of rapid electron and ion transfer. The relationship between the peak current *i* and the scan rate *v* in the CV curve is $i = av^b$,^[46–49] where *b* is a constant between 0.5 and 1.0. The peak area of the CV curve represents the total capacity, which can be divided into diffusion contribution and capacitive contribution according to the equation $i(V) = k_1v + k_2v^{1/2}$.^[50–52] All the *b*-values calculated based on the peak current of redox peaks are close to 1, indicating that Ti₃C₂T_x@MoS₂/NC can provide a large contribution rate of pseudo-capacitance capacity (Figure 5b). The surface-controlled pseudo-capacitance behavior provides a capacity contribution of up to 95.5% at 0.8 mV s⁻¹ (Figure 5c). As the scanning rate was gradually increased from 0.2 to 1.0 mV s⁻¹, the capacity contribution rate provided by the pseudo-capacitor gradually increases from

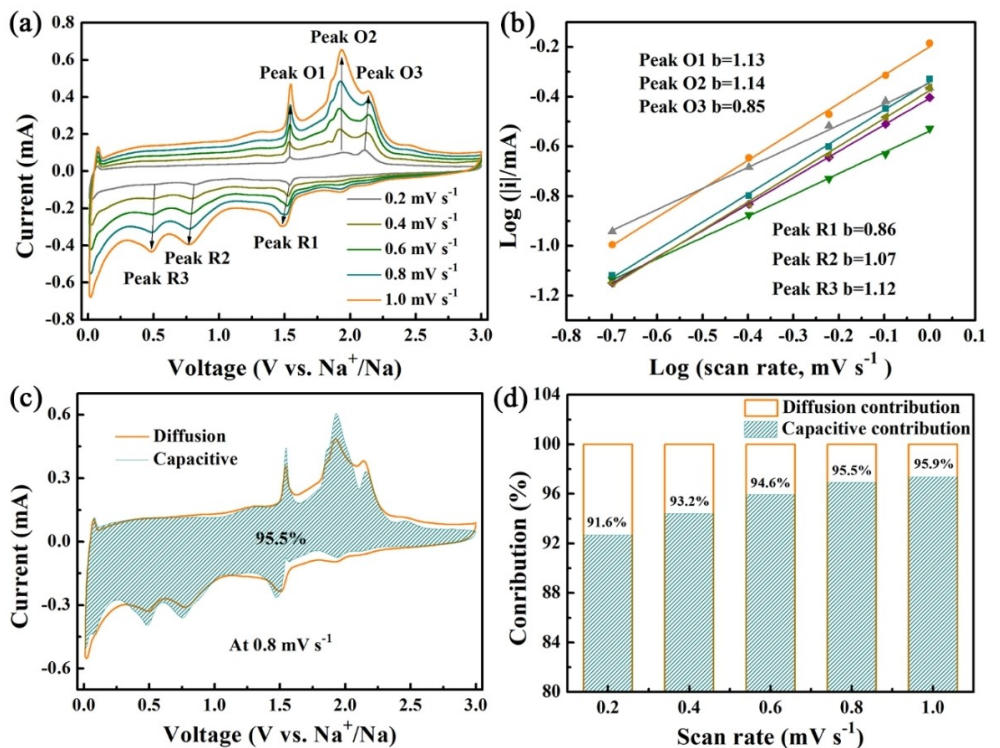


Figure 5. Analysis of pseudo-capacitance behavior of the flower-like $\text{Ti}_3\text{C}_2\text{T}_x@\text{MoS}_2/\text{NC}$: a) CV profiles at different scanning rates, b) b -value, c) capacitive contribution at 1 mV s^{-1} and d) capacitive contribution at various scanning rates.

91.6% to 95.9% (Figure 5d). The $\text{Ti}_3\text{C}_2\text{T}_x@\text{MoS}_2/\text{NC}$ shows a higher pseudo-capacitance contribution compared to $\text{Ti}_3\text{C}_2\text{T}_x$ (Figure S6) thanks to its flower-like hierarchical structure that exposes a larger active surface.

In addition, the reasons for the excellent kinetics of the flower-like $\text{Ti}_3\text{C}_2\text{T}_x@\text{MoS}_2/\text{NC}$ were further analyzed via electrochemical impedance spectroscopy. Figure 6(a) clearly reflects the Nyquist comparison of the $\text{Ti}_3\text{C}_2\text{T}_x$, MoS_2 and flower-like $\text{Ti}_3\text{C}_2\text{T}_x@\text{MoS}_2/\text{NC}$. $\text{Ti}_3\text{C}_2\text{T}_x$ has ultra-high conductivity with a charge transfer resistance (R_{ct}) of only 4.7Ω , whereas the theoretically higher specific capacity of MoS_2 has a R_{ct} of up to 203.4Ω suggesting its poor conductivity. The uniform loading of MoS_2 nanoparticles on the surface of $\text{Ti}_3\text{C}_2\text{T}_x$ nanoflakes

greatly enhanced the electrical conductivity of MoS_2 , and the R_{ct} of the resulting flower-like $\text{Ti}_3\text{C}_2\text{T}_x@\text{MoS}_2/\text{NC}$ is reduced to 73.4Ω , which is attributed to the fact that $\text{Ti}_3\text{C}_2\text{T}_x$ has a high electrical conductivity favoring rapid electron transfer. Figure 6(b) shows the $Z' - \omega^{-1/2}$ linear relationship plots in the low frequency section, and the slope value of the fitted line are the Warburg coefficient (σ_ω) of the electrode materials. The σ_ω values of MoS_2 , $\text{Ti}_3\text{C}_2\text{T}_x$ and the flower-like $\text{Ti}_3\text{C}_2\text{T}_x@\text{MoS}_2/\text{NC}$ are 984, 433 and 337, respectively. The flower-like $\text{Ti}_3\text{C}_2\text{T}_x@\text{MoS}_2/\text{NC}$ takes on the smallest σ_ω value implying that it owns the fastest ion diffusion rate, which is attributed to its 3D flower-like structure provides a smooth ion transport channel for rapid ionic diffusion. $\text{Ti}_3\text{C}_2\text{T}_x@\text{MoS}_2/\text{NC}$ possesses fast charge transfer

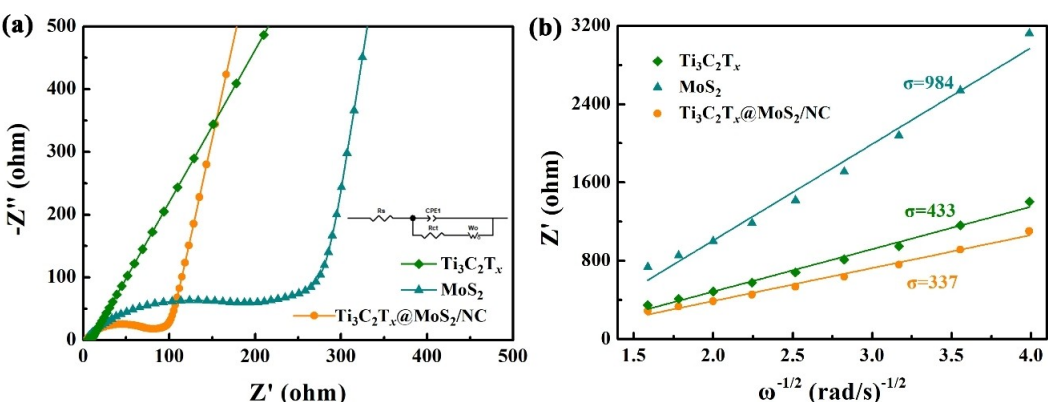


Figure 6. a) Nyquist plots and b) the $Z' - \omega^{-1/2}$ plots of the $\text{Ti}_3\text{C}_2\text{T}_x$, MoS_2 and the flower-like $\text{Ti}_3\text{C}_2\text{T}_x@\text{MoS}_2/\text{NC}$.

kinetics and high ion diffusion capabilities that are conducive to its excellent rate performance and stable reversible cycling.

To further study the practical potential of the flower-like $\text{Ti}_3\text{C}_2\text{T}_x@\text{MoS}_2/\text{NC}$ in practical applications, it was matched with commercial $\text{Na}_3\text{V}_2(\text{PO}_4)_3$ and assembled into a full battery to further evaluate its electrochemical performance, as shown in Figure 7. The sodium storage properties of commercial $\text{Na}_3\text{V}_2(\text{PO}_4)_3$ are shown in Figure S7, and it has excellent cyclic stability. Before assembling a full cell, the flower-like $\text{Ti}_3\text{C}_2\text{T}_x@\text{MoS}_2/\text{NC}$ is assembled into a half cell and subjected to 200 cycles activation at 1 A g^{-1} to achieve a basically stable state. Then, full cell assembly is performed according to the charge matching principle. The capacities of the full cells are determined based on the sum of the masses of the cathode and anode active substances, which are in a mass ratio of approximately 6:1. The full battery achieved a reversible specific capacity of 61 mAh g^{-1} after 120 cycles at 0.2 A g^{-1} corresponding to a capacity retention of 77% (Figure 7a). Figure 7(b) illustrates the GCD profiles of the full cell for the initial 5 cycles. Its first charging and discharging capacity is 85.9 and 79.5 mAh g^{-1} , respectively. The GCD curves of the 2nd to 5th circles basically overlap indicating that the electrode material can reach stabilization very quickly. Figure 7(c) shows a prominent long-term cycling property of the full battery at 0.4 A g^{-1} . The capacity can be kept at 59 mAh g^{-1} after 180 cycles with a small capacity degradation rate of 0.1% each cycle. The superior capacity and recyclability of the full battery can be attributed to the excellent composition and flower-like structure of the $\text{Ti}_3\text{C}_2\text{T}_x@\text{MoS}_2/\text{NC}$ anode, which not only enables the utilization of the individual components but also

effectively speeds up the ion/electron transport rates and the structural stability of the electrode.

Conclusions

In summary, the flower-like $\text{Ti}_3\text{C}_2\text{T}_x@\text{MoS}_2/\text{NC}$ composite have been prepared by complexation of $(\text{MoO}_4)^{2-}$ and dopamine hydrochloride, in-situ polymerization reactions with $\text{Ti}_3\text{C}_2\text{T}_x$ nanosheets and specifies sulfidation. The ultra-small MoS_2 nanoparticles are homogeneously anchored on the surface of the $\text{Ti}_3\text{C}_2\text{T}_x$ nanosheet to form a sandwich-like 2D nanosheet structure, which can not only effectively prevent the $\text{Ti}_3\text{C}_2\text{T}_x$ nanosheets from re-stacking, but also help to shorten the ion diffusion distance, and also help to improve the conductivity of the overall composites. Moreover, the 3D flower-like structure with abundant edges facilitates rapid electrolyte penetration and provides a high contribution of pseudo-capacitance capacity. When employed as anode for SIBs, the $\text{Ti}_3\text{C}_2\text{T}_x@\text{MoS}_2/\text{NC}$ demonstrates excellent cycling stability with capacity retention of 81.4% from 20th cycle to 2000th cycle at 2 A g^{-1} and excellent rate capacity of 383 mAh g^{-1} at 30 A g^{-1} . Meanwhile, the $\text{Ti}_3\text{C}_2\text{T}_x@\text{MoS}_2/\text{NC}||\text{Na}_3\text{V}_2(\text{PO}_4)_3$ full cell exhibits a capacity of 59 mAh g^{-1} at 0.4 A g^{-1} after 180 cycles. This work presents a novel strategy to construct $\text{Ti}_3\text{C}_2\text{T}_x@\text{MoS}_2/\text{NC}$ composite with flower-like structure, as well as may open a new way to construct other MXene-based composites anode materials for SIBs.

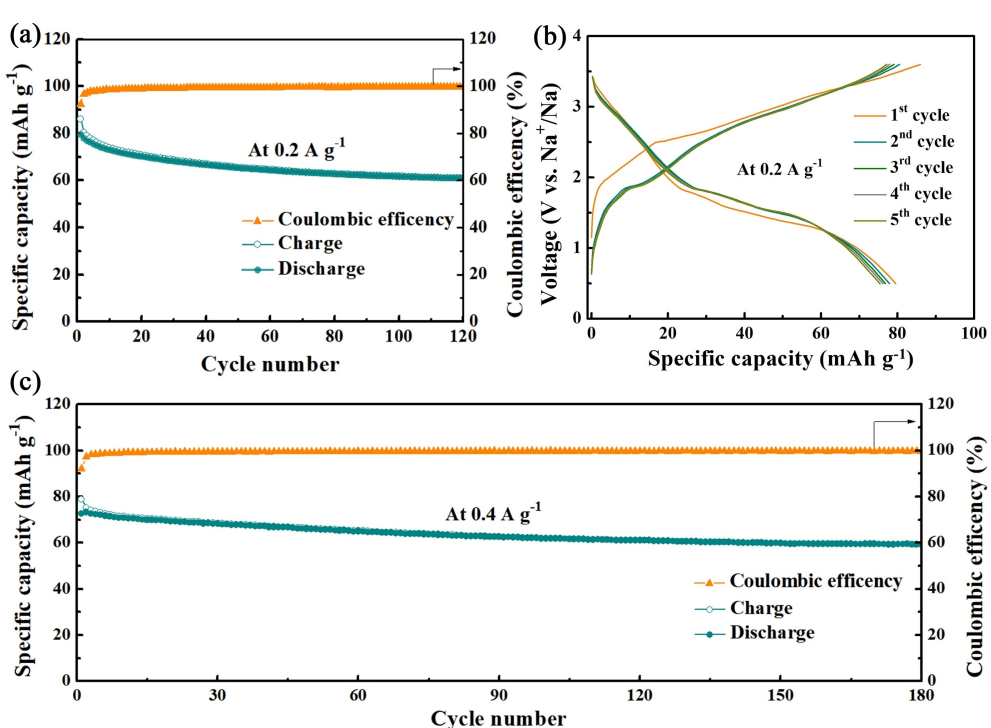


Figure 7. Sodium storage performance of the $\text{Ti}_3\text{C}_2\text{T}_x@\text{MoS}_2/\text{NC}||\text{Na}_3\text{V}_2(\text{PO}_4)_3$ full battery: a) cycling property at 0.2 A g^{-1} , b) initial five GCD profiles at 0.2 A g^{-1} , c) long-term cycling property at 0.4 A g^{-1} .

Experimental Section

Preparation of the $\text{Ti}_3\text{C}_2\text{T}_x$ nanosheets

Few-layer $\text{Ti}_3\text{C}_2\text{T}_x$ was prepared through a modified etching strategy.^[36] Specifically, 2 g of LiF was gradually added to 40 mL of hydrochloric acid (9 mol L^{-1}) with constant stirring until LiF was completely dissolved. Subsequently, 2 g of Ti_3AlC_2 powder was gradually added to the above mixture and stirred continuously at 45°C for 40 h. The $\text{Ti}_3\text{C}_2\text{T}_x$ slurry with multilayer structure was then attained by differential centrifugation and repeated washing with deionized water to $\text{pH} \approx 7$. The multilayer $\text{Ti}_3\text{C}_2\text{T}_x$ was transferred to a wide-mouth bottle, and then a quantity of deionized water was added and ultrasonically stripped under Ar protection for 30 minutes to obtain few-layer $\text{Ti}_3\text{C}_2\text{T}_x$ solution. $\text{Ti}_3\text{C}_2\text{T}_x$ powder can be obtained by freeze-drying few-layer $\text{Ti}_3\text{C}_2\text{T}_x$ solution.

Preparation of the $\text{Ti}_3\text{C}_2\text{T}_x@\text{Mo}/\text{PDA}$ precursor

$\text{Ti}_3\text{C}_2\text{T}_x@\text{Mo}/\text{PDA}$ precursors with different $\text{Ti}_3\text{C}_2\text{T}_x$ contents were prepared by the following strategy. First, different volumes of $\text{Ti}_3\text{C}_2\text{T}_x$ solutions (containing 10, 20 and 40 mg of $\text{Ti}_3\text{C}_2\text{T}_x$, respectively) were measured and diluted to 40 mL, which was denoted as solution A. Then, 0.618 g of $(\text{NH}_4)_6\text{Mo}_7\text{O}_{24} \cdot 4\text{H}_2\text{O}$ and 0.2 g of DA were successively dissolved into 40 mL of water to obtain solution B. Afterward, solution B was dropped into solution A to reach a uniform solution, and then 0.5 mL of $\text{NH}_3 \cdot \text{H}_2\text{O}$ was added to the above mixed solution with constant stirring for 12 hours. Finally, the $\text{Ti}_3\text{C}_2\text{T}_x@\text{Mo}/\text{PDA}$ precursors containing different $\text{Ti}_3\text{C}_2\text{T}_x$ contents were obtained by centrifugation, water washing and freeze-drying.

Preparation of the $\text{Ti}_3\text{C}_2\text{T}_x@\text{MoS}_2/\text{NC}$ composites

A certain mass of $\text{Ti}_3\text{C}_2\text{T}_x@\text{Mo}/\text{PDA}$ precursor and an excess mass of sublimated sulfur (30 times) were weighed and placed at the lower and upper ends of the airflow in the tube furnace, and the final product $\text{Ti}_3\text{C}_2\text{T}_x@\text{MoS}_2/\text{NC}$ was obtained by heating up to 550°C for 2 h with a ramping rate of 5°C min^{-1} under N_2 atmosphere.

Acknowledgements

This work was supported by the Key Laboratory of Superlight Materials and Surface Technology (HEU10202213), the Young Scientists Fund of the National Natural Science Foundation of China (No.12104325), Ministry of Education, High-level scientific research guidance project of Harbin Engineering University-bottleneck research plan (3072022QBZ1004). This work was also supported by the High Performance Research Center of Harbin Engineering University.

Conflict of Interests

The authors declare no conflict of interest.

Data Availability Statement

The data that support the findings of this study are available in the supplementary material of this article.

Keywords: sodium-ion batteries • sandwich complexes • $\text{Ti}_3\text{C}_2\text{T}_x \cdot \text{MoS}_2$ • interlayer spacing

- [1] Z. X. Zhu, T. L. Jiang, M. Ali, Y. H. Meng, Y. Jin, Y. Cui, W. Chen, *Chem. Rev.* **2022**, *122*, 16610–16751.
- [2] G. S. Dong, L. X. Li, K. Zhu, J. Yan, G. L. Wang, D. X. Cao, *Small.* **2023**, *19*, 2208291.
- [3] Y. M. Huang, J. Li, *Adv. Energy Mater.* **2022**, *12*, 2202197.
- [4] K. Wang, H. X. Zhuo, J. T. Wang, F. Poon, X. L. Sun, B. W. Xiao, *Adv. Funct. Mater.* **2023**, *33*, 2212607.
- [5] P. Greim, A. A. Solomon, C. Breyer, *Nat. Commun.* **2020**, *11*, 4570.
- [6] A. Rudola, R. Sayers, C. J. Wright, J. Barker, *Nat. Energy* **2023**, *8*, 215–218.
- [7] G. J. Li, S. G. Guo, B. Xiang, S. X. Mei, Y. Zheng, X. M. Zhang, B. Gao, P. K. Chu, K. F. Huo, *Energy Mater.* **2022**, *2*, 200020.
- [8] J. J. Mu, Z. M. Liu, Q. S. Lai, D. Wang, X. W. Gao, D. R. Yang, H. Chen, W. B. Luo, *Energy Mater.* **2022**, *2*, 200043.
- [9] D. Saurel, B. Orayech, B. W. Xiao, D. Carriazo, X. L. Li, Teófilo Rojo, *Adv. Energy Mater.* **2018**, *8*, 1703268.
- [10] M. Wahid, D. Puthusseri, Y. Gawli, N. Sharma, S. Ogale, *ChemSusChem.* **2018**, *11*, 506–526.
- [11] N. Zhang, X. J. Chen, J. H. Xu, P. F. He, X. L. Ding, *ACS Appl. Mater. Interfaces* **2023**, *15*, 26728–26736.
- [12] J. Yang, J. B. Li, J. H. Lu, X. X. Sheng, Y. Liu, T. T. Wang, C. Y. Wang, *J. Colloid Interface Sci.* **2023**, *649*, 234–244.
- [13] S. Y. Qiao, Q. W. Zhou, M. Ma, H. K. Liu, S. X. Dou, S. K. Chong, *ACS Nano* **2023**, *12*, 11220–11252.
- [14] H. Zhang, I. Hasa, S. Passerini, *Adv. Energy Mater.* **2018**, *8*, 1702582.
- [15] L. C. Wang, J. Swiatowska, S. R. Dai, M. L. Cao, Z. C. Zhong, Y. Shen, M. K. Wang, *Mater. Today Energy* **2019**, *11*, 46–60.
- [16] M. S. Balogun, Y. Luo, W. T. Qiu, P. Liu, Y. X. Tong, *Carbon* **2016**, *98*, 162–178.
- [17] M. M. Lao, Y. Zhang, W. B. Luo, Q. Y. Yan, W. P. Sun, S. X. Dou, *Adv. Mater.* **2017**, *29*, 1700622.
- [18] Y. Z. Jiang, M. J. Hu, D. Zhang, T. Z. Yuan, W. P. Sun, B. Xu, M. Yan, *Nano Energy* **2014**, *5*, 60–66.
- [19] M. K. Nikhil Chandran, G. N. Suresh Babu, M. Sathish, *J. Energy Storage* **2023**, *65*, 107346.
- [20] L. X. Li, C. Wang, C. H. Zhang, X. Q. Cao, J. W. Bai, R. Q. Li, *J. Energy Storage* **2023**, *66*, 107504.
- [21] M. Z. Ma, Y. Yao, Y. Wu, Y. Yu, *Adv. Fiber Mater.* **2020**, *2*, 314–337.
- [22] X. F. Huang, K. H. Tao, T. L. Han, J. J. Li, H. G. Zhang, C. Q. Hu, J. J. Niu, J. Y. Liu, *Small* **2023**, *19*, 302706.
- [23] Y. N. Wei, Z. R. Wang, J. L. Wang, W. Bai, Y. Zhang, B. Y. Liu, *J. Colloid Interface Sci.* **2023**, *638*, 524–541.
- [24] M. Yang, X. Q. Chang, L. Q. Wang, X. Y. Wang, M. Y. Gu, H. Huang, L. Y. Tang, Y. R. Zhong, H. Xia, *Adv. Mater.* **2023**, *35*, 2208705.
- [25] P. Ma, D. L. Fang, Y. L. Liu, Y. Shang, Y. M. Shi, H. Y. Yang, *Adv. Sci.* **2021**, *8*, 2003185.
- [26] Y. T. Wu, P. Nie, J. Wang, H. Dou, X. G. Zhang, *ACS Appl. Mater. Interfaces* **2017**, *9* (45), 39610–39617.
- [27] Y. J. Lei, Z. C. Yan, W. H. Lai, S. L. Chou, Y. X. Wang, H. K. Liu, S. X. Dou, *Electrochem. Energy Rev.* **2020**, *3*, 766–792.
- [28] S. J. Sun, Z. L. Xie, Y. R. Yan, S. P. Wu, *Chem. Eng. J.* **2019**, *366*, 460–467.
- [29] X. Q. Xie, M. Q. Zhao, B. Anasori, K. Maleski, C. E. Ren, J. W. Li, B. W. Byles, E. Pomerantseva, G. X. Wang, Y. Gogotsi, *Nano Energy* **2016**, *26*, 513–523.
- [30] L. Zhang, L. Li, H. L. He, C. X. Liu, J. Dai, Z. Fang, R. M. Wang, D. Chen, *J. Power Sources* **2023**, *574*, 233144.
- [31] Z. Y. Yuan, L. L. Wang, D. D. Li, J. M. Cao, W. Han, *ACS Nano* **2021**, *15*, 7439–7450.
- [32] Z. X. Yuan, H. N. Guo, Y. K. Huang, W. Q. Li, Y. F. Liu, K. Chen, M. Y. Yue, Y. J. Wang, *Chem. Eng. J.* **2022**, *429*, 132394.
- [33] P. F. Huang, H. J. Ying, S. L. Zhang, Z. Zhang, W. Q. Han, *Chem. Eng. J.* **2022**, *429*, 132396.
- [34] Z. Y. Yuan, J. M. Cao, S. Valerii, H. Xu, L. L. Wang, W. Han, *Chem. Eng. J.* **2022**, *430*, 132755.

- [35] Z. M. Liu, S. Tao, J. C. Han, Z. Y. Gao, W. B. Xu, H. H. Min, X. D. Shen, H. Yang, *J. Wang, Mater. Today Energy* **2023**, *33*, 101256.
- [36] M. Ghidiu, M. R. Lukatskaya, M. Q. Zhao, Y. Gogotsi, M. W. Barsoum, *Nature* **2014**, *516*, 78–81.
- [37] L. X. Li, G. S. Dong, H. Zhao, Y. M. Xu, X. F. Zhang, X. L. Cheng, S. Gao, L. H. Huo, *J. Colloid Interface Sci.* **2021**, *586*, 11–19.
- [38] T. Y. Wang, S. Q. Chen, H. Pang, H. G. Xue, Y. Yu, *Adv. Sci.* **2017**, *4*, 1600289.
- [39] Y. Z. Fang, R. Hu, K. Zhu, K. Ye, J. Yan, G. L. Wang, D. X. Cao, *Adv. Funct. Mater.* **2020**, *30*, 2005663.
- [40] B. Q. Ye, L. Xu, W. B. Wu, Y. L. Ye, Z. X. Yang, J. W. Ai, Y. L. Qiu, Z. P. Gong, Y. Q. Zhou, Q. C. Huang, Z. H. Shen, F. S. Li, T. L. Guo, S. Xu, *J. Mater. Chem. C* **2022**, *10*, 3329–3342.
- [41] W. Q. Yu, C. Y. Zhu, R. T. Wang, J. C. Chen, Q. Y. Liu, S. X. Zhang, S. B. Zhang, J. F. Sun, L. W. Yin, *Energy Environ. Mater.* **2022**, *0*, 1–10.
- [42] B. R. Jia, Q. Y. Yu, Y. Z. Zhao, M. L. Qin, W. Wang, Z. W. Liu, C. Y. Lao, Y. Liu, H. W. Wu, Z. L. Zhang, X. H. Qu, *Adv. Funct. Mater.* **2018**, *28*, 1803409.
- [43] B. W. Zhang, S. N. Li, H. L. Yang, X. H. Liang, W. H. Lai, S. L. Zhao, J. C. Dong, S. Q. Chu, Q. F. Gu, J. Liang, Y. Du, X. Xu, L. Y. Cao, Y. X. Wang, F. Pan, S. L. Chou, H. K. Liu, S. X. Dou, *Cell Rep. Phys. Sci.* **2021**, *2*, 100531.
- [44] D. P. Qiu, J. Y. Guan, M. Li, C. H. Kang, J. Y. Wei, Y. Li, Z. Y. Xie, F. Wang, R. Yang, *Adv. Funct. Mater.* **2019**, *29*, 1903496.
- [45] W. Luo, F. Li, J. J. Gaumet, P. Magri, S. Dilberto, L. Zhou, L. Q. Mai, *Adv. Energy Mater.* **2018**, *8*, 1703237.
- [46] C. Liu, B. W. Wang, L. Q. Xu, K. Y. Zou, W. T. Deng, H. S. Hou, G. Q. Zou, X. B. Ji, *ACS Appl. Mater. Interfaces* **2023**, *15*, 5387–5398.
- [47] P. Cai, R. Y. Momen, Y. Tian, L. W. Yang, K. Y. Zou, A. Massoudi, W. T. Deng, H. S. Hou, G. Q. Zou, X. B. Ji, *Adv. Energy Mater.* **2022**, *12*, 2103221.
- [48] X. H. Xiao, X. G. Duan, Z. R. Song, X. G. Deng, W. T. Deng, H. S. Hou, R. J. Zheng, G. Q. Zou, X. B. Ji, *Adv. Funct. Mater.* **2022**, *32*, 2110476.
- [49] Z. R. Song, G. Y. Zhang, X. L. Deng, Y. Tian, X. H. Xiao, W. T. Deng, H. S. Hou, G. Q. Zou, X. B. Ji, *Adv. Funct. Mater.* **2022**, *32*, 2205453.
- [50] X. Yu, F. Hu, Z. Q. Guo, L. Liu, G. H. Song, K. Zhu, *Rare Met.* **2022**, *41*, 29–36.
- [51] C. Guan, F. Hu, X. Yu, H. L. Chen, G. H. Song, K. Zhu, *Rare Met.* **2022**, *41*, 448–456.
- [52] Z. Gong, Z. Li, P. F. Wang, K. Jiang, Z. W. Bai, K. Zhu, J. Yan, K. Ye, G. L. Wang, D. X. Cao, G. H. Chen, *Energy Mater. Adv.* **2023**, *4*, 0035.

Manuscript received: September 8, 2023

Revised manuscript received: November 12, 2023

Accepted manuscript online: November 21, 2023

Version of record online: December 14, 2023